Observation of quantum-limited heat conduction over macroscopic distances

Matti Partanen, Kuan Yen Tan, Joonas Govenius, Russell E. Lake, Miika K. Mäkelä, Tuomo Tanttu, and Mikko Möttönen
QCD Labs, COMP Centre of Excellence, Department of Applied Physics, Aalto University, P.O. Box 13500, FI–00076 Aalto, Finland

(Dated: October 15, 2015)

The emerging quantum technological apparatuses[1,2], such as the quantum computer[3–5], call for extreme performance in thermal engineering at the nanoscale[6]. Importantly, quantum mechanics sets a fundamental upper limit for the flow of information and heat, which is quantified by the quantum of thermal conductance[7,8]. The physics of this kind of quantum-limited heat conduction has been experimentally studied for lattice vibrations, or phonons[9], for electromagnetic interactions[10], and for electrons[11]. However, the short distance between the heat-exchanging bodies in the previous experiments hinders the applicability of these systems in quantum technology. Here, we present experimental observations of quantum-limited heat conduction over macroscopic distances extending to a metre. We achieved this striking improvement of four orders of magnitude in the distance by utilizing microwave photons travelling in superconducting transmission lines. Thus it seems that quantum-limited heat conduction has no fundamental restriction in its distance. This work lays the foundation for the integration of normal-metal components into superconducting transmission lines, and hence provides an important tool for circuit quantum electrodynamics[12–14], which is the basis of the emerging superconducting quantum computer[15]. In particular, our results demonstrate that cooling of nanoelectronic devices can be carried out remotely with the help of a far-away engineered heat sink. In addition, quantum-limited heat conduction plays an important role in the contemporary studies of thermodynamics such as fluctuation relations and Maxwell's demon[16,17]. Here, the long distance provided by our results may, for example, lead to an ultimate efficiency of mesoscopic heat engines with promising practical applications[18].

arXiv:1510.03981v1 [cond-mat.mes-hall] 14 Oct 2015

The quantum of thermal conductance, G_{Q}, provides the fundamental upper limit for heat conduction through a single channel[7]. This limit applies to fermions and bosons as the carriers of heat as well as to so-called anyons obeying even more general statistics[8]. Although a few observations of quantum-limited heat conduction have been reported, the studied distances were shorter than 100 μm in all previous experiments: phononic heat conduction through four parallel submicrometre dielectric wires each supporting four vibrational modes[9], electromagnetic heat conduction in a superconducting loop over a 50-μm distance[10,19], and electronic heat conduction through an extremely short quantum point contact engineered in a two-dimensional electron gas[11]. Photons, unlike many other carriers of heat, can travel macroscopic distances without significant scattering, for example, in optical fibres or superconducting waveguides. Thus, photons seem ideal for long-distance thermal engineering and provide attractive opportunities for various quantum thermodynamics experiments[16]. To our knowledge, however, itinerant photons have not been previously employed in experimental studies of the quantum of thermal conductance.

In this Letter, we experimentally study heat conduction through a single channel formed by photons travelling in a long superconducting waveguide in a single transverse mode. This scheme supports a photonic thermal conductance very close to G_{Q}. Since this heat transport does not directly depend on the temperature of the substrate phonons, it provides an efficient method for remote temperature control. The superconducting waveguide is terminated at both ends by resistors composed of mesoscopic normal-metal islands (Islands A and B in Fig. 1). We measure the temperatures of the Islands A and B, and vary the temperature of Island B. A characteristic signal of photonic heat transport in our experiments is the increasing response of the temperature of Island A to the controlled temperature changes of Island B with decreasing phonon bath temperature (Figs. 2 and 3). The measured temperatures well agree with the thermal model, implying that the heat conduction essentially reaches the quantum limit. Furthermore, the most important features of the measurement results can be quantitatively predicted from a theoretical model involving no free parameters (Fig. 3). These observations constitute firm evidence of quantum-limited heat conduction over macroscopic distances.

Figure 1 shows the structure of the sample used in the experiments together with the measurement scheme. We study several samples with different parameters as presented in Table I. The length of the coplanar waveguide is either 20 cm or 1 m, and it has a double-spiral structure on a silicon chip with the size of 1×1 cm^2 or 2×2 cm^2, respectively. The electron temperatures of the normal-metal islands are measured and controlled with the help of normal-metal–insulator–superconductor (NIS) junctions (Methods). There are four nominally identical NIS junctions at each island. In all samples, the normal-metal islands terminating the waveguide have two galvanic contacts to superconducting lines: one to the centre conductor of the waveguide and the other to the ground plane. The waveguide has a centre conductor width of 10 μm, and a separation between the ground plane and the centre conductor of 5 μm. In the control

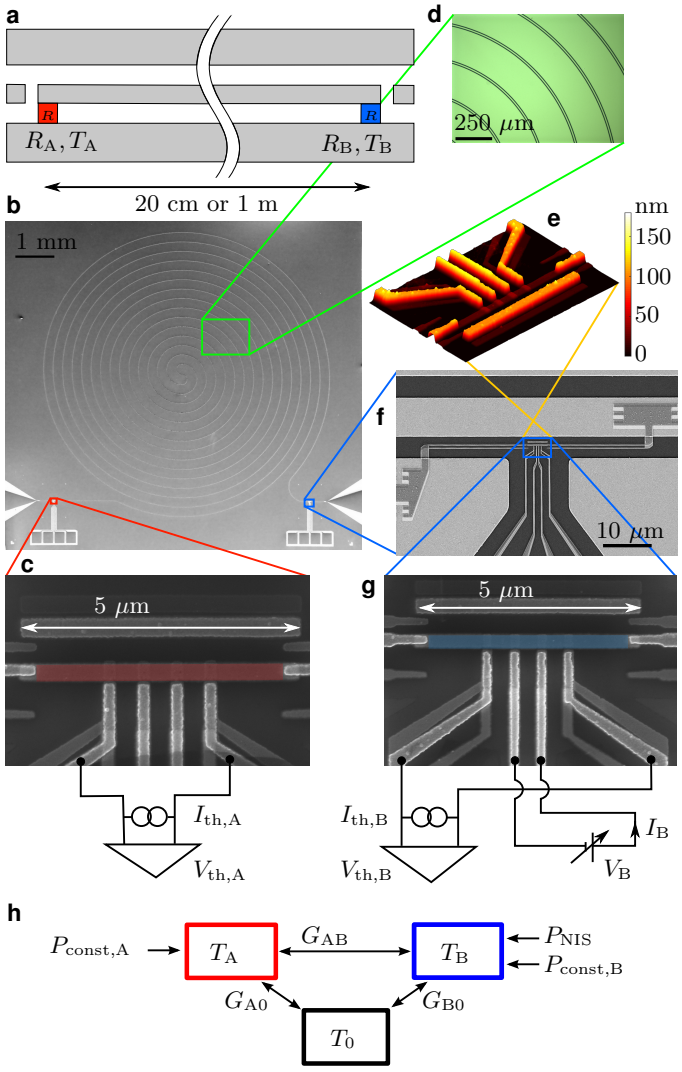

FIG. 1 | Sample structure and measurement scheme. **a**, Schematic illustration of a coplanar transmission line terminated at different ends by resistances R_A and R_B at temperatures T_A and T_B, respectively. **b**, Scanning electron microscope (SEM) image of a fabricated transmission line with a double-spiral structure. **c, g**, False-colour SEM images of the normal-metal islands together with a simplified measurement scheme. **d**, Optical micrograph of the waveguide. **e**, Atomic force microscope image of Island B highlighting the thicknesses of the nanostructures. **f**, SEM image showing how the normal-metal island is connected to the ground plane and to the centre conductor. **h**, Thermal model indicating the thermal conductance between the Islands A and B, G_{AB}, and those from the islands to the phonon bath at the temperature T_0, G_{A0} and G_{B0}. Constant powers $P_{const,A/B}$ and control power P_{NIS} are also indicated by arrows. Micrographs (**c, e, f, g**) are from Sample A1, and (**b, d**) are from a similar sample.

sample, the centre conductor is shunted to ground to extinguish photonic heat conduction (Fig. 6).

All measurements are performed at millikelvin temperatures. The voltage-biased (V_B) NIS junctions at Island B are used for temperature control whereas the current-biased ($I_{th,A}$, $I_{th,B}$) junctions at both islands are used for thermometry. The thermometer calibration data for Sample A1 is shown in Fig. 5b, c. Here, we focus mainly on the analysis of Sample A1, which exhibits the highest photonic thermal conductance according to the model. It also achieves the lowest electron temperature, below 90 mK at the 10-mK base temperature of the cryostat. The other samples show higher minimum electron temperatures, which increases the uncertainty in their thermometry at the very low temperatures.

TABLE I | **Main parameters of the measured samples.** Columns show the waveguide lengths, normal-metal resistances R_i, $i \in \{A, B\}$, normal-metal materials, and normal-metal volumes (length×width×thickness). Furthermore, G_Γ/G_Q provides the estimated ratio of the realised photonic thermal conductance and the quantum of thermal conductance at temperatures of approximately 150 mK.

Sample	Length (m)	R_i (Ω)	Material	Volume (nm^3)	G_Γ/G_Q
A1	0.2	65	Cu	5000 × 300 × 20	98 %
A2	1.0	75	AuPd	3200 × 300 × 40	94 %
A3	0.2	150	AuPd	3200 × 300 × 20	60 %
Control	0.2	100	AuPd	3200 × 300 × 20	0 %

We analyse the thermal conductance between the Islands A and B, G_{AB}, and those to the phonon bath, G_{A0} and G_{B0}, as schematically presented in Fig. 1h. By linearising the heat flows of Island A at small temperature differences, energy conservation yields a differential temperature response: $dT_A/dT_B = G_{AB}/(G_{AB} + G_{A0})$. If the conductance G_{AB} between the islands is quantum limited and the heat conduction to the bath stems from qualitatively different phenomena, G_{AB} dominates over G_{A0} at low enough temperatures. Thus, the temperature response generally tends to unity with decreasing temperatures.

The photonic net power flow from normal-metal Island A to B is given by (Methods and Ref. 20)

$$P_\Gamma = \int_0^\infty \frac{d\omega}{2\pi} \hbar\omega |t(\omega)|^2 \left[\frac{1}{\exp(\frac{\hbar\omega}{k_B T_A}) - 1} - \frac{1}{\exp(\frac{\hbar\omega}{k_B T_B}) - 1} \right] \quad (1)$$

where $\hbar$ is the reduced Planck constant, k_B is the Boltzmann constant, and $|t(\omega)|^2$ is a transmission coefficient that depends on the photon angular frequency ω, the characteristic impedance of the transmission line, and the resistances of the terminating normal-metal islands (see Eq. 9 for details). If the characteristic impedance of the transmission line equals the island resistances, we have $|t(\omega)|^2 = 1$. In this case, an analytical solution is obtained, $P_\Gamma = \frac{\pi k_B^2}{12\hbar}(T_A^2 - T_B^2)$, which can further be expressed in terms of the quantum of thermal conductance as $P_\Gamma = G_Q(T_A - T_B)$, where $G_Q = \frac{\pi k_B^2 T}{6\hbar}$ with $T = (T_A + T_B)/2$. The thermal conductance to the

phonon bath at temperature T_0 can be approximated by the electron–phonon conductance as $G_{A0} \approx G_{ep,A} = 5\Sigma_N \Omega_A T_0^4$ in Island A (Methods). Here, Σ_N is a material parameter describing the strength of the electron–phonon coupling in the normal metal, and Ω_A is the volume of Island A. Thus, one obtains a simple theoretical prediction without any free parameters based on quantum-limited photonic heat conduction and electron–phonon coupling

$$\frac{dT_A}{dT_B} = \frac{1}{1 + aT_0^3} \quad (2)$$

where $a = 30\Sigma_N \Omega_A \hbar/(\pi k_B^2)$ is a predetermined constant. We also devise a full thermal model shown in Fig. 5a for a more accurate description of the heat flows (Methods).

Figure 2 shows the measured island temperatures for Sample A1 at various bath temperatures together with the corresponding results from the full thermal model. The experimental observations are in good agreement with the simulations over a wide range of bath temperatures and bias voltages. The maximum cooling of Island B is obtained at its bias voltages $V_B \lesssim 2\Delta/e \approx 0.45$ mV, where Δ is the superconductor energy gap and e is the elementary charge. The clearly observed cooling of distant Island A cannot be attributed to phonons since the phonon bath temperature increases as a result of the net heating power $|V_B I_B|$ dissipated during cooling of Island B. In addition to photons, quasiparticles may contribute to the heat conduction, but their effect is weak and qualitatively in contradiction with our observations at low temperatures[19]. Furthermore, the essentially vanishing temperature response for the control sample in Fig. 2f indicates that the photonic channel dominates in the heat conduction between the islands in Sample A1.

To accurately analyse the photonic heat conduction, we show the temperature of Island A in Fig. 3a as a function of the electron temperature of Island B for different bath temperatures. The measured temperatures of Island A in Fig. 3a are insensitive to heat conduction mechanisms that only involve Island B and its reservoirs. Therefore, this analysis method provides a robust way of studying photonic heat conduction. In Sample A1, the curvatures of T_A as a function of T_B are negative, which is in stark contrast to the positive curvature observed for the control sample. This fundamental difference is due to the absense of the photonic heat conduction in the control sample. In Samples A2 and A3 (Table I), the curvatures resemble that of A1 (data not shown). At high bath temperatures, T_A is almost independent of T_B, which is a consequence of the strong electron–phonon coupling. Figure 3b shows the differential temperature response, dT_A/dT_B, extracted at the lowest T_B obtained for each bath temperature. The steep increase in dT_A/dT_B at low bath temperatures is a signature of the photonic heat conduction: the thermal conductance between the islands, G_{AB}, determined by the photonic heat conduction, dominates over the conductance to the bath, G_{A0}.

In addition, Fig. 3b shows a prediction of the simplified

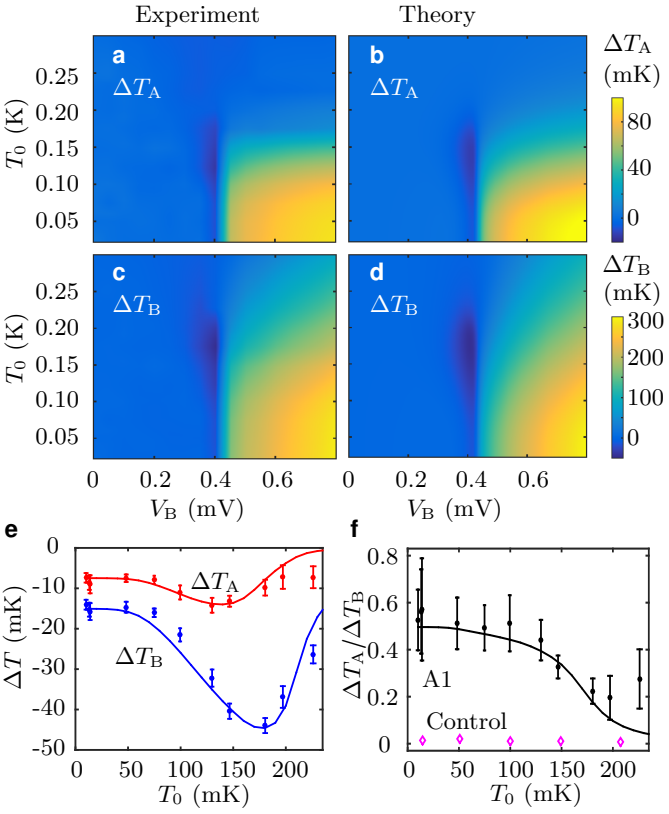

FIG. 2 | Photonic cooling at macroscopic distances for Sample A1. **a, b**, Measured and theoretically predicted electron temperature changes with respect to the zero-bias case ($V_B = 0$) for Island A as functions of the voltage V_B and bath temperature T_0. **c, d**, As in panels (**a, b**), but for temperature changes of Island B. **e**, Measured (markers) and simulated (lines) temperature changes at the maximum cooling point as functions of the bath temperature. The errorbars indicate the standard deviation of the measured temperatures. **f**, The ratio of the temperature changes in (**e**). In addition, measurement results from the control sample are shown for comparison.

model according to Eq. 2. Despite its simplicity, it captures the essential features of the experimental data of Samples A1 and A2 which exhibit photonic heat conduction very close to the quantum limit, G_Q. The deviation between the data and the simplified model at high temperatures is due to the neglected quasiparticle heat conduction between the islands and their reservoirs which increases G_{A0}. At low temperatures, on the other hand, the discrepancy increases due to the saturation of the electron temperatures not present in the simplified model. These observations bring insight to the good agreement between the experimental observations and the full thermal model.

In summary, we experimentally demonstrate quantum-limited heat conduction over macroscopic distances. The on-chip design of the resistors enables their straightforward utilisation in a multitude of different applications, including the initialization of quantum bits[21] by con-

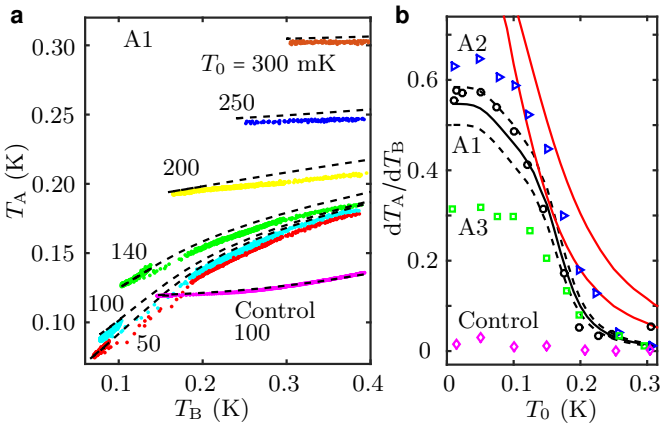

FIG. 3 | Differential temperature response and the quantum of thermal conductance. **a**, Measured (dots) and simulated (dashed lines) temperatures of Island A as functions of the temperature of Island B for the indicated phonon bath temperatures in Sample A1. The results for the control sample at 100 mK bath temperature are shown for comparison. **b**, Differential temperature response (●) from (**a**) at the lowest T_B for each bath temperature. The experimental uncertainty is of the order of the marker size. For comparison, we also show the corresponding experimental data for the control sample (◊), for Sample A2 (▷), and for A3 (□). The solid black line shows the prediction of the full thermal model of Fig. 5a. The dashed lines are calculated with 80 % (bottom) and 115 % (top) of the quantum of thermal conductance indicating the sensitivity of the results to the photonic heat conduction. The solid red lines are calculated with the simplified thermal model [Eq. (2)] for Sample A1 without any free parameters: we take into account only quantum-limited photonic heat conduction and electron–phonon coupling with literature values[6] for the constant of Cu, $\Sigma_N = 2\times10^9$ WK^{-5}m^{-3} (right), and $\Sigma_N = 4\times10^9$ WK^{-5}m^{-3} (left).

trolled cooling and remote cooling of other quantum-technological components. The methods developed in this study may also be used in the future to implement efficient heat transfer between separate chips and temperature stages of the cryostat. For example, the remotely cooled quantum device may be operated at a typical base temperature whereas the cold reservoir may be located at a lower-temperature stage which is incompatible with the relatively large power consumption of the actual device. The cooling distance we demonstrate here is sufficient for practically all present-day applications.

METHODS

Sample fabrication

The samples are fabricated in a multi-step process on 0.5-mm-thick silicon wafers with 300-nm-thick thermally grown silicon oxide layers. The transmission lines are fabricated in an optical-lithography process using a mask aligner and an electron beam evaporator. The wafers are cleaned with reactive ion etching before the metal deposition. The Al film has a thickness of 200 nm, on top of which films of Ti and Au are deposited with thicknesses of 3 and 5 nm, respectively, to prevent oxidation.

The nanostructures are fabricated with electron beam lithography. The mask consists of poly(methyl methacrylate) and poly[(methyl methacrylate)-*co*-(methacrylic acid)] layers, which enable a large undercut necessary for three-angle shadow evaporation. Prior to the metal deposition, the samples are cleaned with argon plasma in the electron beam evaporator. As the first metal, we deposit an Al layer which is oxidised *in situ* introducing the insulator layer for the NIS junctions. Subsequently, a layer of normal metal is deposited followed by a layer of Al. The normal metal is either AuPd (mass ratio 3:1) or Cu. Lift-off of the excess metal is performed with acetone followed by cleaning with isopropanol.

Measurements

The electrical measurements are performed at millikelvin temperatures achieved with a commercial cryogen-free dilution refrigerator. The chip is attached to a sample holder containing a printed circuit board (PCB), to which the sample is connected by Al bond wires. The PCB is connected to room-temperature measurement setup with lossy coaxial cables. To suppress electrical noise, the power-line-powered devices are connected to the sample through opto-isolators. Battery-powered amplifiers and voltage and current sources are connected to the sample without opto-isolation. The voltage V_B is swept slowly (down to 1 μV/s) to avoid apparent hysteresis. Furthermore, the measurements are repeated several times, and the data points with clear disturbance from random external fluctuations are excluded.

Photonic heat conduction

Here, we derive Eq. (1) for the photonic heat conduction starting from the first-principles circuit quantum electrodynamics. Previously, our case of two islands coupled with a transmission line has been studied with the help of classical circuit theory[20]. These results can also be obtained using paht integrals[17]. In contrast, we analyse the system using methods discussed in ref. 22. In particular, the Heisenberg equations of motion are given by Kirchhoff's circuit laws. Furthermore, a terminating resistor can be treated as a semi-infinite transmission line with a characteristic impedance equal to its resistance[22].

We express the boundary conditions originating from the Kirchhoff's laws for the photon annihilation operators defined in Fig. 4 as

$$\frac{1}{\sqrt{Z_0}}(\hat{b}_L - \hat{b}_R) = -\frac{1}{\sqrt{R_A}}(\hat{a}_R - \hat{a}_L) \quad (3)$$

$$\frac{1}{\sqrt{Z_0}}(\hat{c}_R - \hat{c}_L) = -\frac{1}{\sqrt{R_B}}(\hat{d}_L - \hat{d}_R) \quad (4)$$

$$\sqrt{Z_0}(\hat{b}_L + \hat{b}_R) = \sqrt{R_A}(\hat{a}_R + \hat{a}_L) \quad (5)$$

$$\sqrt{Z_0}(\hat{c}_R + \hat{c}_L) = \sqrt{R_B}(\hat{d}_L + \hat{d}_R) \quad (6)$$

$$\hat{c}_R = e^{i\phi}\hat{b}_R \quad (7)$$

$$\hat{b}_L = e^{i\phi}\hat{c}_L \quad (8)$$

where $\phi = \omega s/v$ is the phase shift obtained by a wave with angular frequency ω and velocity v when travelling over distance s. Assuming no photons coming from the right, $\hat{d}_\mathrm{L} = 0$, we can solve the transmission coefficient t defined as $\hat{d}_\mathrm{R} = t(\omega)\hat{a}_\mathrm{R}$. Thus, we obtain

$$|t(\omega)|^2 = \frac{2}{1 + \frac{R_\mathrm{A}^2+R_\mathrm{B}^2}{2R_\mathrm{A}R_\mathrm{B}} + \frac{R_\mathrm{A}^2R_\mathrm{B}^2+Z_0^4-R_\mathrm{A}^2Z_0^2-R_\mathrm{B}^2Z_0^2}{2R_\mathrm{A}R_\mathrm{B}Z_0^2}\sin^2(\phi)} \quad (9)$$

The transmission coefficient is symmetric with respect to the exchange of resistances R_A and R_B. In a matched case, $R_\mathrm{A} = R_\mathrm{B} = Z_0$, Eq. (9) simplifies to $|t(\omega)|^2 = 1$.

Energy dissipation at the resistor R_B can be obtained from the average photon flux to the right in the transmission line with a characteristic impedance R_B multiplied by the energy carried by each photon. Here, the zero-point energy does not appear in the dissipated power. Thus, the power per unit frequency can be expressed as

$$\begin{aligned} P_{\rightarrow,\omega} &= \langle \hbar\omega \hat{d}_\mathrm{R}^\dagger \hat{d}_\mathrm{R}\rangle \\ &= \hbar\omega|t(\omega)|^2\langle \hat{a}_\mathrm{R}^\dagger \hat{a}_\mathrm{R}\rangle \\ &= \hbar\omega|t(\omega)|^2 \frac{1}{\exp(\frac{\hbar\omega}{k_B T_\mathrm{A}}) - 1} \end{aligned} \quad (10)$$

since the number of photons emitted by the left resistor is given in thermal equilibrium by the Bose–Einstein distribution. Due to symmetry, the power transfer to the opposite direction is given by

$$P_{\leftarrow,\omega} = \hbar\omega|t(\omega)|^2 \frac{1}{\exp(\frac{\hbar\omega}{k_B T_\mathrm{B}}) - 1} \quad (11)$$

The net photonic heat transport from R_A to R_B is, therefore, given by

$$\begin{aligned} P_\Gamma &= \int_0^\infty \frac{\mathrm{d}\omega}{2\pi}(P_{\rightarrow,\omega} - P_{\leftarrow,\omega}) \\ &= \int_0^\infty \frac{\mathrm{d}\omega}{2\pi}\hbar\omega|t(\omega)|^2 \left[\frac{1}{\exp(\frac{\hbar\omega}{k_B T_\mathrm{A}}) - 1} - \frac{1}{\exp(\frac{\hbar\omega}{k_B T_\mathrm{B}}) - 1}\right] \end{aligned} \quad (12)$$

In the special case of a vanishing waveguide length, $s \to 0$, Eq. (9) yields $|t(\omega)|^2 = 4R_\mathrm{A}R_\mathrm{B}/(R_\mathrm{A}+R_\mathrm{B})^2$ which is identical to the result considered in ref. 23 for two resistors in a loop. On the other hand, if one sets Z_0 to be inversely proportional to s and takes the limit $s \to 0$, one obtains $|t(\omega)|^2 = 4R_\mathrm{A}R_\mathrm{B}/[(R_\mathrm{A}+R_\mathrm{B})^2 + X^2]$ with a reactance $X = Z_0\omega s/v$. This result reproduces that of two resistances connected in a loop with a series reactance[20,23].

NIS thermometry

The quasiparticle current through an NIS junction with tunnelling resistance R_T is given in the sequential-tunnelling theory by[6]

$$I(V,T_\mathrm{N}) = \frac{1}{eR_\mathrm{T}}\int_0^\infty n_S(E)[f(E-eV,T_\mathrm{N}) - f(E+eV,T_\mathrm{N})]\mathrm{d}E \quad (13)$$

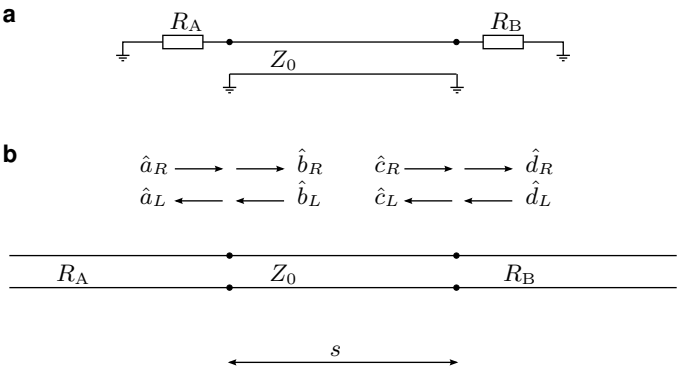

FIG. 4 | Transmission line diagrams. a, Circuit diagram of a transmission line with characteristic impedance Z_0 terminated by resistors R_A and R_B. **b**, System in (**a**) represented as three connected transmission lines. The annihilation operators for the left- and right-moving photons at the different points of the system are denoted by $\hat{a}_i, \hat{b}_i, \hat{c}_i$, and $\hat{d}_i$, $i \in \{\mathrm{L},\mathrm{R}\}$.

where T_N is the normal-metal electron temperature, and V the voltage across the junction. Here, the Fermi–Dirac distribution is given by

$$f(E,T) = \frac{1}{e^{E/(k_\mathrm{B}T)} + 1} \quad (14)$$

and the superconductor density of quasiparticle states assumes the form

$$n_\mathrm{S}(E) = \left|\mathrm{Re}\frac{E/\Delta + i\gamma}{\sqrt{(E/\Delta + i\gamma)^2 - 1}}\right| \quad (15)$$

Above, γ is the Dynes parameter[6] accounting for the subgap current, and Δ is the superconductor energy gap. Experimentally, γ is obtained as the ratio of the asymptotic resistance at large voltages and the resistance at zero voltage. We note that Eq. (13) has a very weak dependence on the temperature of the superconductor through the temperature dependence of Δ. Thus, an NIS junction can be used as a thermometer probing the electron temperature of the normal-metal. We apply a constant current, and deduce the temperature from the measured voltage according to a calibration curve shown in Fig. 5.

Thermal model

In the full thermal model illustrated in Fig. 5a, we consider several heat transfer mechanisms: Firstly, the NIS junctions produce heat flows between the normal-metal islands and the superconducting leads. Secondly, the electrons in the normal metal exchange heat with the phonon bath. Thirdly, the islands exchange heat with each other by photons travelling in the transmission line. Finally, the model takes into account geometrical properties of the samples as well as properties specific to the measurement setup.

The NIS junctions can be used for cooling and heating of the normal metal, and the power out of the normal

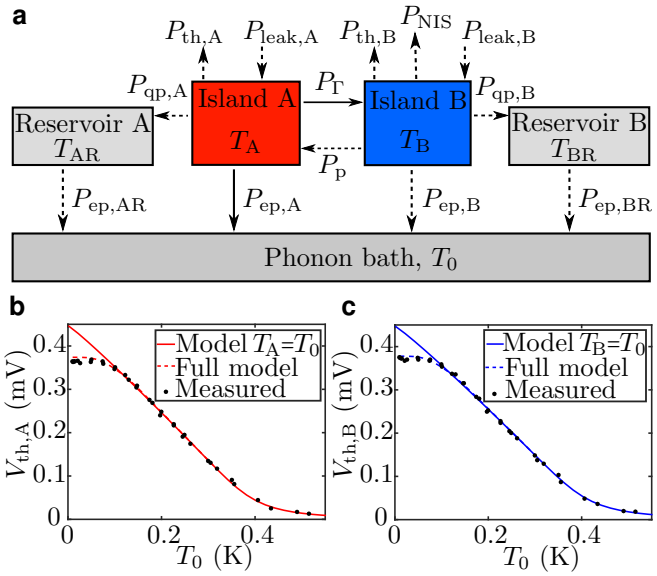

FIG. 5 | Thermal model and temperature calibration. **a**, In the full thermal model, the conduction electron systems of the normal-metal islands exchange heat with each other by photonic heat conduction, P_Γ, and with the near-by normal-metal reservoirs through quasiparticle heat conduction, $P_{{\rm qp},i}$. The electrons exchange heat directly with the phonon bath through the electron–phonon coupling $P_{{\rm ep},i}$. The temperature of Island B is controlled with power of the NIS junction, $P_{\rm NIS}$, and the thermometers introduce powers $P_{{\rm th},i}$. Heat leakages from a high-temperature environment, $P_{{\rm leak},i}$, are also included in the model as well as a parasitic heat flow between the islands, $P_{\rm p}$. Here, subscripts A, B, AR, and BR denote Islands A and B, and the corresponding reservoirs, respectively. The simplified model accounts only for P_Γ and $P_{\rm ep,A}$, which are denoted by solid arrows. See Methods for details. **b, c**, Thermometer voltages as defined in Figs. 1c, g for Island A (**b**) and B (**c**) as functions of the bath temperature in Sample A1. The solid lines show theoretical predictions without any free parameters assuming that the electron temperature is equal to the bath temperature. These curves are used for the voltage–temperature conversion. The discrepancy between the data and the model below 100 mK indicates the saturation of the electron temperature, confirmed by the dashed lines showing the theoretically predicted voltages with the electron temperature solved from the full thermal model. The uncertainty in the measurements is of the order of the marker size.

metal can be computed from[6]

$$P_{\rm ideal}=\frac{1}{e^2R_{\rm T}}\int_{-\infty}^{\infty}n_{\rm S}(E)(E-eV)[f(E-eV,T_{\rm N})-f(E,T_{\rm S})]{\rm d}E \tag{16}$$

We model the nonidealities in the NIS power by assuming a constant fraction, β, of the power flowing to the superconductor to flow back to the normal metal. Thus, the back-flow power can be written as

$$P_{\rm bf}=\beta(IV+P_{\rm ideal}) \tag{17}$$

where IV gives the total power. Consequently, the total cooling power of an NIS junction is given by

$$P_{\rm NIS}=P_{\rm ideal}-P_{\rm bf} \tag{18}$$

The physical background for the back flow has been studied in ref. 24. A factor of 2 is included in the power when two NIS junctions are connected to form an SINIS structure. Since the thermometers are based on similar NIS junctions, their powers are calculated with the same equations as for the actual power used to control the temperature of Island B. However, the voltages across the thermometer junctions must first be solved using Eq. (13), the island temperature and the thermometer bias current.

The electrons in the normal metal are coupled to the phonon bath, and the heat flow is given by[6]

$$P_{{\rm ep},i}=\Sigma_{\rm N}\Omega_i(T_i^5-T_0^5) \tag{19}$$

Here, Ω_i is the volume of normal-metal block $i\in\{{\rm A, B, AR, BR}\}$. For Cu and AuPd, the parameter $\Sigma_{\rm N}$ is typically[6,19] between 2×10^9 and 4×10^9 WK^{-5}m^{-3}. In the simulations, we use values 2.0×10^9 WK^{-5}m^{-3} and 3.0×10^9 WK^{-5}m^{-3} for Cu and AuPd, respectively, unless otherwise mentioned. The normal metal under the superconductors at the ends of the islands are excluded from the volume in the simulations due to the superconductor proximity effect. For small temperature differences, $T_i\approx T_0$, one obtains

$$P_{{\rm ep},i}=G_{{\rm ep},i}(T_i-T_0) \tag{20}$$

where $G_{{\rm ep},i}=5\Sigma_{\rm N}\Omega_iT_0^4$.

We account for heat leaks from a high-temperature environment by including constant heating powers to both islands, $P_{\rm leak,A}$ and $P_{\rm leak,B}$. They are fixed by the saturation of the electron temperature observed in Fig. 5 at low bath temperatures.

In the thermal model, we consider quasiparticle heat conduction only from the islands to their near-by normal-metal reservoirs. The reservoirs are a consequence of the three-angle evaporation method, and they provide an additional channel for thermalisation to the phonon bath. At both islands, there are actually two reservoirs which are presented as one in Fig. 5a for simplicity. The extremely weak quasiparticle heat conduction from one island to the other over a distance longer than 5 mm is included in the parasitic heat conduction as discussed below. The power flow at the normal-metal block i due to the quasiparticles is given by[19]

$$P_{{\rm qp},i}=\kappa_{\rm S}AT'(x_i) \tag{21}$$

where $T'(x_i)$ is the derivative of the temperature in the superconductor with respect to the position coordinate x_i, and A is the cross section of the line. The superconductor heat conductivity, $\kappa_{\rm S}$, is related to the normal-state heat conductivity, $\kappa_{\rm N}$, at a temperature T by[25]

$$\kappa_{\rm S}=\tilde{\gamma}(T)\kappa_{\rm N} \tag{22}$$

where $\tilde{\gamma}$ is a suppression factor

$$\tilde{\gamma}(T) = \frac{3}{2\pi^2}\int_{\Delta/(k_\mathrm{B}T)}^{\infty}\frac{t^2}{\cosh^2(t/2)}\mathrm{d}t \quad (23)$$

The normal-state heat conductivity of the line is obtained from the Wiedemann–Franz law as

$$\kappa_\mathrm{N} = \frac{L_0 T(x)}{\rho} \quad (24)$$

where ρ is the normal-state electric resistivity of the line, and $L_0 = 2.4\times10^{-8}$ WΩK^2 is the Lorenz number. The temperature profile in the superconducting lines can be calculated using a heat diffusion equation[19]. However, the electron–phonon coupling in a superconducting state is greatly suppressed with respect to that of a normal-state[26]. Thus, we neglect the electron–phonon coupling in the leads and assume here a linear temperature profile.

Andreev current plays a minor role in our experiments since the induced temperature changes at the islands are small in the subgap voltage regime where it may dominate[27]. Therefore, we do not consider it in the thermal model.

We observe a weak island-to-island heat transport also in the control sample, in which the centre conductor is shunted as shown in Fig. 6. We model this parasitic heat transport by letting a constant proportion, α, of the total input power at Island B to flow into Island A,

$$P_\mathrm{p} = \alpha I_\mathrm{B} V_\mathrm{B} \quad (25)$$

The exact mechanism of the parasitic channel remains unknown, and the heat flow may depend on the sample geometry. The parasitic heat conduction extracted from the control sample includes all the heat conduction channels from one island to the other except the photonic heat conduction which is essentially absent due to the shunt. This heat flow may be attributed to quasiparticles since they can travel long distances before recombination, especially at low bath temperatures. Furthermore, although the electric contact of the shunting metal block between the ground plane and the centre conductor is of very low impedance, small residual photonic heat conduction cannot be fully excluded. Nevertheless, the parasitic heat conduction is much weaker than the total heat conduction in the actual devices. We note that the parasitic heat conduction is only added to the model for more accurate description at high heating powers.

We solve the heat balance equations for both islands and both reservoirs simultaneously. The equations can be expressed as (Fig. 5a)

$$P_\Gamma + P_\mathrm{th,A} - P_\mathrm{leak,A} - P_\mathrm{p} + P_\mathrm{ep,A} + P_\mathrm{qp,A} = 0 \quad (26)$$
$$P_\mathrm{NIS} - P_\Gamma + P_\mathrm{th,B} - P_\mathrm{leak,B} + P_\mathrm{p} + P_\mathrm{ep,B} + P_\mathrm{qp,B} = 0 \quad (27)$$
$$P_\mathrm{ep,AR} - P_\mathrm{qp,A} = 0 \quad (28)$$
$$P_\mathrm{ep,BR} - P_\mathrm{qp,B} = 0 \quad (29)$$

These equations yield the temperatures T_i, $i \in \{\mathrm{A}, \mathrm{B}, \mathrm{AR}, \mathrm{BR}\}$ for a given phonon bath temperature, T_0, and bias voltage, V_B, both of which are accurately controlled.

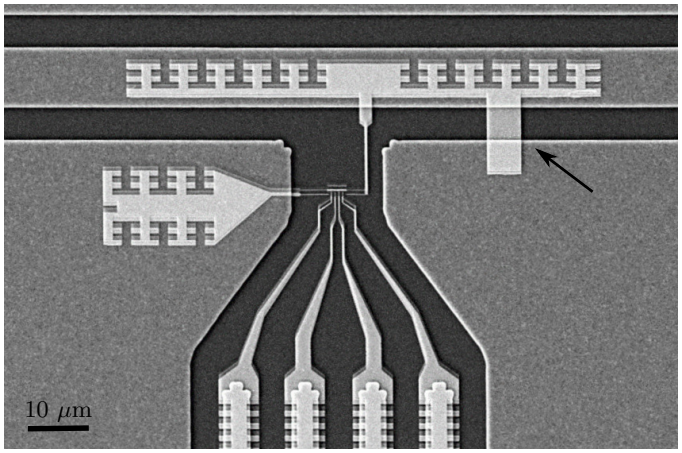

FIG. 6 | Control sample. SEM image of the control sample. The center conductor of the coplanar waveguide is shunted to the ground plane at the location indicated by the black arrow.

The parameters used in the full thermal model are shown in Table II. In the simulations, we slightly adjust the quasiparticle heat conductivity for improved agreement between the model and the experiments. More specifically, we set the temperature in Eq. (23) to be equal to the island temperatures increased by a small constant value and, in addition, we set the suppression factor to saturate at low temperatures. Hence, we introduce a replacement $\tilde{\gamma}(T) \to \tilde{\gamma}(T+T_\mathrm{const})+\tilde{\gamma}(T_\mathrm{satur})$. This approximation can be justified by several arguments. Firstly, the superconductor heat conductivity depends on the purity of the sample[29]. Secondly, the superconductor energy gap has been observed to increase at small film thicknesses[30]. We use for all superconductors the same value, which is obtained from the current–voltage measurements of the NIS junctions, although the leads are thicker. The possibly smaller actual energy gap effectively corresponds to higher temperatures. Thirdly, the neglected electron–phonon coupling in the superconducting leads may result in nonlinear temperature profile increasing the quasiparticle heat conduction. The impurities in the sample may increase the electron–phonon coupling. Fourthly, the heat leakage through the measurement cables from a high-temperature environment and other possible heat leak mechanisms may increase the temperature of the superconductors. Increased quasiparticle densities have been observed previously, and they can be suppressed by effective shielding and enhanced relaxation[31]. Weak quasiparticle recombination can induce elevated quasiparticle temperatures. However, we increase only the heat conductivity and consider a linear temperature profile in the lead between the island and the near-by reservoir. In the simulations, the reservoirs have effective volumes somewhat larger than their physical volumes, thus, taking into account the quasiparticles thermalising in the reservoirs and the ones recombining

TABLE II | **Simulation parameters for Sample A1.** Sample dimesions are based on the actual sample, $I_{\mathrm{th,A}}$ and $I_{\mathrm{th,B}}$ are externally controlled, Δ, γ and resistances are extracted from independent current–voltage characteristics, ρ assumes a typical value for evaporated aluminium, L_l is calculated analytically[28], C_l is based on a finite-element simulation, $P_{\mathrm{leak,A}}$ and $P_{\mathrm{leak,B}}$ are obtained from island temperature saturation at low phonon bath temperatures in Fig. 5, α is extraced from the control sample, β is obtained from the nonideal cooling power of the NIS junctions, Ω_{AR} and Ω_{BR} are the actual volumes multiplied by 2 to account also for the quasiparticle recombination in the superconductors, and T_{satur} and T_{const} are fitting parameters assuming realistic values.

Parameter	Symbol	Value	Unit
Island volume	Ω_{A}, Ω_{B}	$4500 \times 300 \times 20$	nm^3
Effective reservoir volume	$\Omega_{\mathrm{AR}}, \Omega_{\mathrm{BR}}$	$10 \times \Omega_{\mathrm{A}}$	
Cross section of lines from island to reservoir	A	300×100	nm^2
Distance from island to reservoir	l_{IR}	24	μm
Waveguide length	s	0.193	m
Superconductor energy gap	Δ	224	μeV
Inductance per unit length	L_l	4.14×10^{-7}	H/m
Capacitance per unit length	C_l	1.51×10^{-10}	F/m
Thermometer bias current	$I_{\mathrm{th,A}}$, $I_{\mathrm{th,B}}$	18	pA
Resistivity of Al lines in normal state	ρ	1.0×10^{-8}	Ωm
Dynes parameter	γ	1.05×10^{-4}	
Material parameter for Cu	Σ_{N}	2.0×10^{9}	$\mathrm{W\ K^{-5}\ m^{-3}}$
Normal state junction resistance	R_{T}	15.5	kΩ
Island resistance	R_{A}, R_{B}	65	Ω
Characteristic impedance	Z_0	$\sqrt{L_l/C_l}$	
Phase velocity	v	$1/\sqrt{C_l L_l}$	
Lorenz number	L_0	2.4×10^{-8}	$\mathrm{W\ \Omega\ K^{-2}}$
Saturation quasiparticle temperature for heat conductivity	T_{satur}	0.184	K
Additional quasiparticle temperature for heat conductivity	T_{const}	0.036	K
Parasitic heat conduction parameter	α	3×10^{-4}	
NIS back flow constant	β	0.056	
Heat leak	$P_{\mathrm{leak,A}}$, $P_{\mathrm{leak,B}}$	1.6	fW

in the superconductors. The requirement of the effective volume may also be explained by the uncertainty in the employed literature value of the electron–phonon coupling constant[6].

Additional control samples without resistors

We also fabricated and measured control samples without the normal-metal resistors terminating the transmission line. Instead, the transmission line is connected to input and output ports through coupling capacitors. The capacitors and the transmission line form a resonator, the quality factor of which can be measured. Using an LCR model[28], we extract the internal quality factor of the system to be of the order of 60,000 indicating a negligibly weak effect in the heat conduction experiments. In fact, the energy losses due to the observed finite quality factor would only limit the photonic heat conduction beyond distances of the order of a kilometer.

[1] Wolf, E. L. *Quantum Nanoelectronics: An Introduction to Electronic Nanotechnology and Quantum Computing* (Wiley-VCH, Weinheim, 2009).

[2] Dowling, J. P. & Milburn, G. J. Quantum technology: the second quantum revolution. *Philosophical Transactions of the Royal Society of London A: Mathematical, Physical and Engineering Sciences* **361**, 1655–1674 (2003).

[3] Ladd, T. D. *et al.* Quantum computers. *Nature* **464**, 45–53 (2010). URL `http://dx.doi.org/10.1038/nature08812`.

[4] Clarke, J. & Wilhelm, F. K. Superconducting quantum bits. *Nature* **453**, 1031–1042 (2008). URL `http://dx.doi.org/10.1038/nature07128`.

[5] Morton, J. J. L., McCamey, D. R., Eriksson, M. A. & Lyon, S. A. Embracing the quantum limit in silicon computing. *Nature* **479**, 345–353 (2011). URL `http://dx.doi.org/10.1038/nature10681`.

[6] Giazotto, F., Heikkilä, T. T., Luukanen, A., Savin, A. M. & Pekola, J. P. Opportunities for mesoscopics in thermome-

try and refrigeration: Physics and applications. *Rev. Mod. Phys.* **78**, 217–274 (2006). URL http://link.aps.org/doi/10.1103/RevModPhys.78.217.

[7] Pendry, J. B. Quantum limits to the flow of information and entropy. *J. Phys. A: Math. Gen.* **16**, 2161 (1983). URL http://stacks.iop.org/0305-4470/16/i=10/a=012.

[8] Rego, L. G. C. & Kirczenow, G. Fractional exclusion statistics and the universal quantum of thermal conductance: A unifying approach. *Phys. Rev. B* **59**, 13080–13086 (1999). URL http://link.aps.org/doi/10.1103/PhysRevB.59.13080.

[9] Schwab, K., Henriksen, E. A., Worlock, J. M. & Roukes, M. L. Measurement of the quantum of thermal conductance. *Nature* **404**, 974–977 (2000). URL http://dx.doi.org/10.1038/35010065.

[10] Meschke, M., Guichard, W. & Pekola, J. P. Single-mode heat conduction by photons. *Nature* **444**, 187–190 (2006). URL http://dx.doi.org/10.1038/nature05276.

[11] Jezouin, S. *et al.* Quantum limit of heat flow across a single electronic channel. *Science* **342**, 601–604 (2013). URL http://www.sciencemag.org/content/342/6158/601.abstract. http://www.sciencemag.org/content/342/6158/601.full.pdf.

[12] Blais, A., Huang, R.-S., Wallraff, A., Girvin, S. M. & Schoelkopf, R. J. Cavity quantum electrodynamics for superconducting electrical circuits: An architecture for quantum computation. *Phys. Rev. A* **69**, 062320 (2004). URL http://link.aps.org/doi/10.1103/PhysRevA.69.062320.

[13] Wallraff, A. *et al.* Strong coupling of a single photon to a superconducting qubit using circuit quantum electrodynamics. *Nature* **431**, 162–167 (2004). URL http://dx.doi.org/10.1038/nature02851.

[14] Astafiev, O. *et al.* Resonance fluorescence of a single artificial atom. *Science* **327**, 840–843 (2010). URL http://www.sciencemag.org/content/327/5967/840.abstract. http://www.sciencemag.org/content/327/5967/840.full.pdf.

[15] Kelly, J. *et al.* State preservation by repetitive error detection in a superconducting quantum circuit. *Nature* **519**, 66–69 (2015). URL http://dx.doi.org/10.1038/nature14270.

[16] Pekola, J. P. Towards quantum thermodynamics in electronic circuits. *Nature Phys.* **11**, 118–123 (2015). URL http://dx.doi.org/10.1038/nphys3169.

[17] Golubev, D. S. & Pekola, J. P. Statistics of heat exchange between two resistors. *Phys. Rev. B* **92**, 085412 (2015). URL http://link.aps.org/doi/10.1103/PhysRevB.92.085412.

[18] Sothmann, B., Snchez, R. & Jordan, A. N. Thermoelectric energy harvesting with quantum dots. *Nanotechnology* **26**, 032001 (2015). URL http://stacks.iop.org/0957-4484/26/i=3/a=032001.

[19] Timofeev, A. V., Helle, M., Meschke, M., Möttönen, M. & Pekola, J. P. Electronic refrigeration at the quantum limit. *Phys. Rev. Lett.* **102**, 200801 (2009). URL http://link.aps.org/doi/10.1103/PhysRevLett.102.200801.

[20] Pascal, L. M. A., Courtois, H. & Hekking, F. W. J. Circuit approach to photonic heat transport. *Phys. Rev. B* **83**, 125113 (2011). URL http://link.aps.org/doi/10.1103/PhysRevB.83.125113.

[21] Geerlings, K. *et al.* Demonstrating a driven reset protocol for a superconducting qubit. *Phys. Rev. Lett.* **110**, 120501 (2013). URL http://link.aps.org/doi/10.1103/PhysRevLett.110.120501.

[22] Yurke, B. & Denker, J. S. Quantum network theory. *Phys. Rev. A* **29**, 1419–1437 (1984). URL http://link.aps.org/doi/10.1103/PhysRevA.29.1419.

[23] Schmidt, D. R., Schoelkopf, R. J. & Cleland, A. N. Photon-mediated thermal relaxation of electrons in nanostructures. *Phys. Rev. Lett.* **93**, 045901 (2004). URL http://link.aps.org/doi/10.1103/PhysRevLett.93.045901.

[24] O'Neil, G. C., Lowell, P. J., Underwood, J. M. & Ullom, J. N. Measurement and modeling of a large-area normal-metal/insulator/superconductor refrigerator with improved cooling. *Phys. Rev. B* **85**, 134504 (2012). URL http://link.aps.org/doi/10.1103/PhysRevB.85.134504.

[25] Bardeen, J., Rickayzen, G. & Tewordt, L. Theory of the thermal conductivity of superconductors. *Phys. Rev.* **113**, 982–994 (1959). URL http://link.aps.org/doi/10.1103/PhysRev.113.982.

[26] Timofeev, A. V. *et al.* Recombination-limited energy relaxation in a bardeen-cooper-schrieffer superconductor. *Phys. Rev. Lett.* **102**, 017003 (2009). URL http://link.aps.org/doi/10.1103/PhysRevLett.102.017003.

[27] Rajauria, S. *et al.* Andreev current-induced dissipation in a hybrid superconducting tunnel junction. *Phys. Rev. Lett.* **100**, 207002 (2008). URL http://link.aps.org/doi/10.1103/PhysRevLett.100.207002.

[28] Göppl, M. *et al.* Coplanar waveguide resonators for circuit quantum electrodynamics. *J. Appl. Phys.* **104**, – (2008). URL http://scitation.aip.org/content/aip/journal/jap/104/11/10.1063/1.3010859.

[29] Satterthwaite, C. B. Thermal conductivity of normal and superconducting aluminum. *Phys. Rev.* **125**, 873–876 (1962). URL http://link.aps.org/doi/10.1103/PhysRev.125.873.

[30] Court, N. A., Ferguson, A. J. & Clark, R. G. Energy gap measurement of nanostructured aluminium thin films for single cooper-pair devices. *Supercond. Sci. Technol.* **21**, 015013 (2008). URL http://stacks.iop.org/0953-2048/21/i=1/a=015013.

[31] Saira, O.-P., Kemppinen, A., Maisi, V. F. & Pekola, J. P. Vanishing quasiparticle density in a hybrid Al/Cu/Al single-electron transistor. *Phys. Rev. B* **85**, 012504 (2012). URL http://link.aps.org/doi/10.1103/PhysRevB.85.012504.

Acknowledgements We acknowledge the provision of facilities and technical support by Aalto University at Micronova Nanofabrication Centre. We also acknowledge funding by the European Research Council under Starting Independent Researcher Grant No. 278117 (SINGLEOUT), the Academy of Finland through its Centres of Excellence Program (grant no. 251748) and grants (nos 138903, 135794, 265675, 272806 and 276528), the Emil Aaltonen Foundation, the Jenny and Antti Wihuri Foundation and the Finnish Cultural Foundation. We thank M. Meschke, J. P. Pekola, D. S. Golubev, M. Kaivola and J. C. Cuevas for discussions concerning this work. Furthermore, we thank L. Grönberg for assistance in sample fabrication, and E. Mykkänen and A. Kemppinen for assistance in measurements.

Author Contributions M.P. and K.Y.T. fabricated the samples, developed and conducted the experiments, and analysed the data. J.G., R.E.L. and M.K.M. assisted in the sample fabrication and measurements. T.T. con-

tributed to the measurements. M.M. provided the initial ideas and suggestions for the experiment and supervised the work in all respects. All authors discussed both experimental and theoretical results and commented on the manuscript that was written by M.P. and M.M.

Author Information Correspondence and requests for materials should be addressed to M.M. (mikko.mottonen@aalto.fi).